Boron and phosphorus doped diamond: change in the electronic structure post exposure to low pressure deuterium plasma and its effect on the production of negative ions

Ryan Magee, Marie-Amandine Pinault-Thaury, Jocelyn Achard, Jean-Marc Layet, Didier Guyomarc'H, Marco Minissale, Timo Gans, James Dedrick, Gilles Cartry

▶ To cite this version:

Ryan Magee, Marie-Amandine Pinault-Thaury, Jocelyn Achard, Jean-Marc Layet, Didier Guyomarc'H, et al.. Boron and phosphorus doped diamond: change in the electronic structure post exposure to low pressure deuterium plasma and its effect on the production of negative ions. Journal of Physics D: Applied Physics, 2025, 58 (18), pp.185208. ⟨10.1088/1361-6463/adc270⟩. ⟨hal-05172852⟩

HAL Id: hal-05172852

https://hal.science/hal-05172852v1

Submitted on 21 Jul 2025

Journal of Physics D:
Applied Physics

PURPOSE-LED
PUBLISHING™

PAPER • OPEN ACCESS

Boron and phosphorus doped diamond: change in the electronic structure post exposure to low pressure deuterium plasma and its effect on the production of negative ions

To cite this article: Ryan Magee *et al* 2025 *J. Phys. D: Appl. Phys.* **58** 185208

View the article online for updates and enhancements.

OPEN ACCESS
IOP Publishing
Journal of Physics D: Applied Physics
J. Phys. D: Appl. Phys. **58** (2025) 185208 (13pp)
https://doi.org/10.1088/1361-6463/adc270

Boron and phosphorus doped diamond: change in the electronic structure post exposure to low pressure deuterium plasma and its effect on the production of negative ions

Ryan Magee[1,*], Marie-Amandine Pinault-Thaury[2], Jocelyn Achard[3], Jean-Marc Layet[4], Didier Guyomar'ch[4], Marco Minissale[4], Timo Gans[5], James P Dedrick[1] and Gilles Cartry[4]

[1] York Plasma Institute, School of Physics, Engineering and Technology, University of York, Heslington, York YO10 5DD, United Kingdom
[2] GEMaC-CNRS/UVSQ, Université Paris-Saclay, Versailles, France
[3] LSPM-CNRS, UPR 3407, Université Sorbonne Paris Nord, 99 Avenue J. B. Clément, Villetaneuse F-93439, France
[4] Aix-Marseille University - CNRS, PIIM UMR 7345, Centre de St Jérôme, Marseille Cedex 20 13397, France
[5] School of Physical Sciences, National Centre for Plasma Science and Technology, Faculty of Science and Health, Dublin City University, Dublin, Ireland

E-mail: ryan.magee@york.ac.uk

Received 13 September 2024, revised 11 March 2025
Accepted for publication 19 March 2025
Published 7 April 2025

Abstract

Negative ion production is of significant interest for materials processing and neutral beam injection systems for magnetic confinement fusion reactors. The surface production mechanism can be required for high current applications. Dielectric materials, including doped diamond, are of interest for increasing surface production as a potential alternative to low-work function metals and further understanding of the underpinning mechanisms is needed. In this study we use photoemission yield spectroscopy, in conjunction with the Fowler model and mass spectrometry, to measure the negative ion yield and ionization threshold of micro-crystalline diamond (μc-D), micro-crystalline boron doped diamond (μc-BDD) and single crystal phosphorus doped diamond (PDD) under deuterium plasma exposure at sample temperatures between 30 °C and 700 °C. We observe that deuterium plasma exposure of PDD at 400 °C reduces its ionization threshold from approximately 4.0 eV to 2.1 eV, which is similar to the work function of cesium. While the ionization threshold of diamond is observed to be sensitive

---

[*] Author to whom any correspondence should be addressed.

to sample temperature and the dopant used, this appears to have negligible effect on negative ion production. Developing a better understanding of which material properties are most significant for negative ion production will assist the development of improved negative ion sources.

Keywords: deuterium plasma, negative ions, surface production, electronic properties

1. Introduction

Negative ions play a significant role in the chemistry and physics of electronegative plasmas and are relevant for materials processing [1, 2], particle acceleration [3–6] and ion thrusters [7–9]. They are also of interest for neutral beam injection systems (NBIs) in magnetic confinement fusion reactors [10–14].

To produce the high densities of negative ions necessary for NBIs, surface production from caesiated materials is typically employed due to their low work function [15, 16]. The use of cesium introduces significant engineering challenges [11, 15, 17] and therefore other materials such as electrides [18] and dielectrics [19–21] are being studied as potential alternatives. Dielectrics are of interest due to the reduced losses of negative ions back to the surface as compared to conductive materials [19]. This is as a result of their bandgap which prevents the electrons captured by the negative ions from returning to the surface as their affinity level overlaps with forbidden states in the bandgap.

One dielectric of particular interest for negative ion production is diamond. While the erosion of diamond under deuterium plasma exposure [22] is a drawback for its use in negative ion sources, it is an ideal material for investigation due to the relative ease with which doping can be used to customize its electronic properties. The negative ion yield from diamond, graphite, and the electride C12A7 has been estimated to be approximately 3%, significantly higher than that of metallic tungsten or molybdenum at below 1% but still an order of magnitude below caesiated molybdenum at approximately 30% [23]. The negative ion yield variation under deuterium plasma exposure of micro-crystalline diamond (μc-D) [19, 21], p-type boron doped diamond (μc-BDD) [24–26] and n-type micro-crystalline nitrogen doped diamond (μc-NDD) [20, 21] have all previously been investigated.

N-type phosphorus doped diamond (PDD) is a promising material for the surface production of negative ions and thermionic emission applications [27, 28] due to its dopant level being just 0.6 eV below the conduction band [29], which is significantly closer than for μc-NDD at 1.7 eV. This means that at moderate temperatures the number of electrons in the conduction band ready for capture by incoming particles is much larger for PDD than NDD. This has resulted in significant research into its electronic structure and negative electron affinity (NEA) [27, 28, 30–38]. While these properties suggest the possibility of efficient negative ion production, the link between electronic structure and negative ion yield for PDD has yet to be fully investigated.

Negative ions can be produced through the backscattering of incoming positive hydrogen ions or fast neutrals, or alternatively through the sputtering of hydrogen adsorbed onto the surface from the plasma. The number of negative ions produced from a surface is proportional to the product of the ionization energy and the sum of the yields from backscattering and sputtering [39]. These processes can be impacted upon by plasma exposure through the sp^2 (graphite)/sp^3 (diamond) hybridization ratio of the surface (for carbon-based materials), and the incident ion energy. For metals, the ionization probability is exponentially dependent on the work function and as such, the work function is considered to be one of the primary material properties for optimizing negative ion yield from conductors [6, 24, 40, 41]. However, for dielectrics other parameters such as the presence and characteristics of a band gap can play a strong role in the ionization probability and can therefore decrease the importance of the low ionization threshold (known as the work function in metals) [24].

In this study, we use photoemission yield spectroscopy (PYS) and mass spectrometry to link the electronic structure of PDD with negative-ion yield in low-pressure deuterium plasmas. The results are compared with previously investigated μc-D and μc-BDD.

The experimental methods are described in section 2. Results for electronic structure, ionization thresholds and negative ion measurements are presented in section 3.

2. Method

2.1. Plasma source

The experimental setup is shown in figure 1.

The setup is described in detail in [24]. In brief, an inductively coupled plasma is generated in the source region, figure 1(a), which diffuses through a grounded mesh and into the diffusion chamber. The deuterium gas is held at 2 Pa by a scroll pump, a turbo molecular pump, and an adjustable valve.

2.2. Temperature and voltage biasing of the sample

Inside the diffusion chamber figure 1(b), samples are mounted on a heating element of temperature 30 °C–700 °C. Note that ‘room temperature’ measurements refer to measurements in which no heating was applied from the element, due to heating from the plasma, these temperatures can vary between approximately 30 °C and 80 °C. The sample holder can rotate by 180° to face either the mass spectrometer for negative ion measurements, or alternatively towards the tunable light

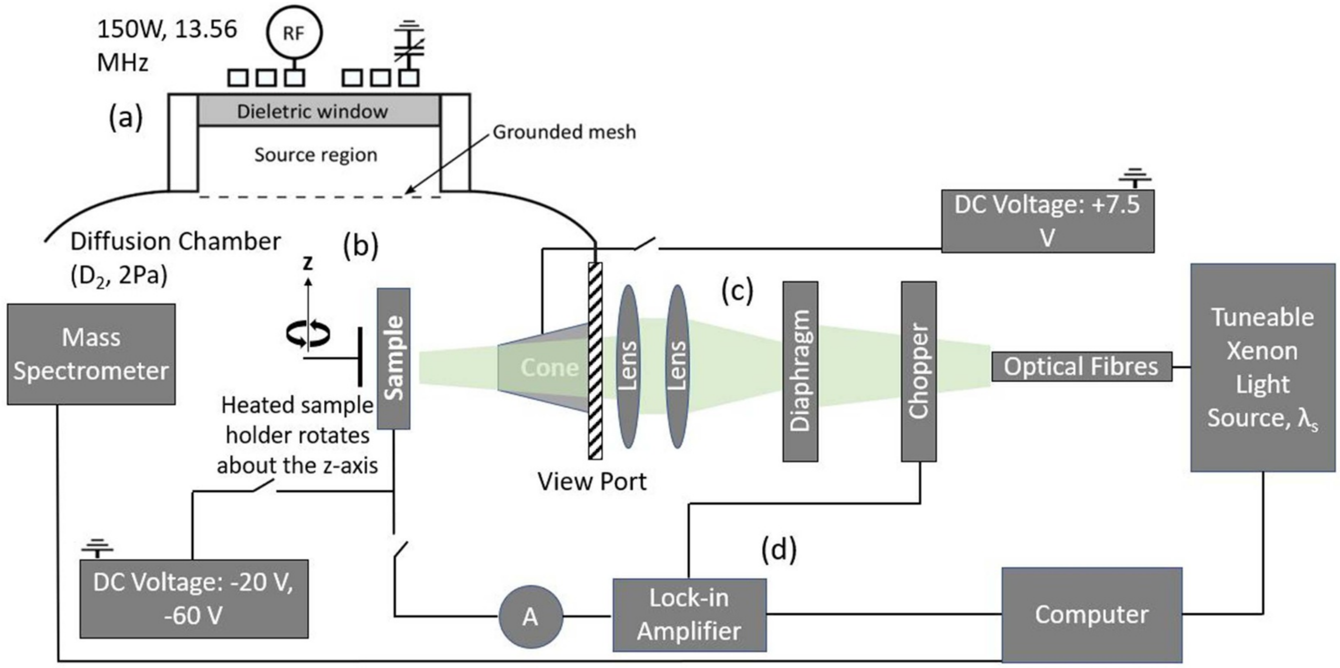

Figure 1. Set up of the experiment. (a) ICP deuterium plasma source, (b) diffusion chamber containing mounted sample with temperature control (30 °C–700 °C), and mass spectrometer (c) optical setup for photoemission yield spectroscopy, and (d) photocurrent measurement system with synchronized chopper and lock-in amplifier. Not drawn to scale.

source for PYS. Sample biases of -20 V and -60 V were chosen to compare negative ion yield with and without a significant sputtering contribution from adsorbed hydrogen atoms onto the sample [39]. Negatively biasing the sample attracts positive ions from the plasma and can lead to a positive charge build up on the surface of non-conductive samples. For this reason pulsed sample biasing has previously been used to allow biasing of non-conductive samples [21]. It has previously been shown that the magnitude of the surface bias is approximately equal to that of the applied pulsed bias for a short enough pulse (for which the positive charge build up is negligible) [42]. Pulsed biasing also limits ion bombardment induced damage to the sample. In order to preserve the electronic properties of the diamond surface as much as possible, the bias voltage was initially limited to -20 V. Subsequently a second set of measurements were undertaken for the large bias voltage of -60 V. The voltage bias was applied during 20 μs pulses with a frequency of 1 kHz and a duty cycle of 2%. These conditions were chosen to minimize both the build up of surface charge and ion bombardment induced damage. During this 20 μs the sample is bombarded by ions having energy on the order of 27 eV, i.e. equivalent to the plasma potential (as measured by a Langmuir probe) minus the bias voltage. The rest of the time the sample is at ground and bombarded by ions having an energy set by the plasma potential, about 7 eV. The main ion D_3^+ dissociates at impact and its fragments share the energy. Therefore the maximum impact energy is 27 eV during the pulse and 7 eV outside the pulse from D^+ impacts. However, most of the impacts occur at 9 eV during the pulse and approximately 2 eV outside the pulse as a result of the impact and fragmentation of D_3^+, splitting the energy equally between the three D atoms or ions.

To confirm that pulsed biasing of the sample at -20 V does not induce more ion bombardment damage than plasma exposure without bias, a PYS measurement, described in section 2.4, was taken for identical experimental conditions and for the same sample both after plasma exposure without bias and with the pulsed bias at -20 V. No significant difference was observed. However, it is important to note that even in the absence of sample biasing, the plasma can influence the diamond surface through chemical sputtering. Indeed, chemical sputtering thresholds have been calculated in [22], and they vary from 2 to 4 eV depending on the sample temperature.

2.3. *Mass spectrometry for the measurement of negative ions*

A mass spectrometer (Hiden EQP 300, orifice 100 μm in diameter) is mounted with its axis perpendicular to the sample at a distance of 38 mm, figure 1(b), and is used to measure negative ions produced at the sample surface. Negative ions are self-extracted from the sample to the mass spectrometer by the application of a negative bias.

The corresponding timing diagram is shown in figure 2.

For negative ion measurements, the electrostatic optics are tuned to optimize the transmission of D^- ions. The voltage is scanned over 35 V to measure the negative ions according to their mass and energy and obtain negative ion energy distribution functions (NIEDFs). The total number of negative ions is

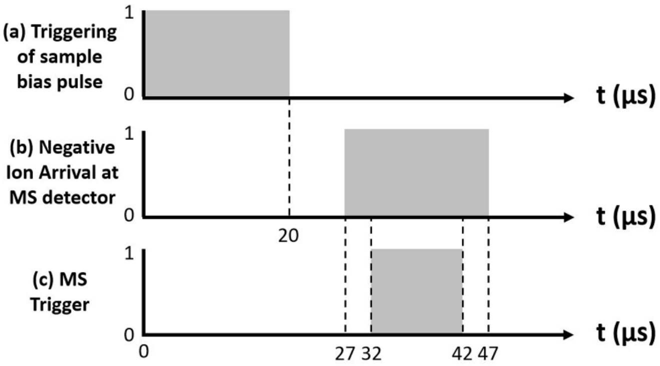

Figure 2. Timing diagram for the synchronization of (a) the pulsing of the sample bias, (b) the arrival of negative ions at the mass spectrometer and (c) the triggering of the mass spectrometer. Not drawn to scale.

determined by integrating under the NIEDF [19]. Over multiple independent measurements we have observed a fluctuation in negative ion counts of approximately 15%, and this is used to give a representative value for uncertainty bars.

2.4. PYS to determine electronic structure and ionization thresholds

2.4.1. Experimental setup. The optical setup and measurement procedure for PYS, shown in figure 1(c), remains unchanged from that in [24], and a brief description is provided here. A 300 W xenon lamp is used in conjunction with a monochromator (Zolix omni-λ 300i) and an optical fiber to expose the sample to an approximately 4 mm diameter monochromatic beam with a tunable wavelength range of 200–1200 nm and a spectral width of 10 nm. This beam passes through a chopper to modulate the photocurrent at 35 Hz. Next, a diaphragm and two lenses are used to focus the beam through a cone and onto the sample. The cone is used to minimize photon reflections onto the sample holder that may result in electron emission and contribute to the measured photocurrent. It is also biased at 7.5 V to attract and collect any emitted electrons.

The current from the sample is converted to a voltage by an ammeter and passed onto the lock-in amplifier which extracts the 35 Hz photocurrent. This detection is synchronized with the scanning wavelength of the incident light and therefore can be used to measure the photocurrent with respect to the wavelength of the incident light.

The diamond samples are introduced under vacuum via a load-lock, annealed for a few minutes at 400 °C to outgas surface adsorbates and then analyzed by PYS prior to plasma exposure. The μc-D and μc-BDD samples are expected to be hydrogen terminated after the deposition process and the annealing temperature used is *a priori* not high enough to outgas hydrogen. The PDD sample is oxygen terminated as a result of an acid cleaning.

2.4.2. Determining the electronic structures of the samples. We follow the previous work of Takeuchi *et al* in [30–38] to determine the electronic structure of the material, for example the band gap and NEA. There are two differences with our setup: (1) they used a channeltron electron multiplier under ultra-high vacuum conditions to detect the photoemitted electrons, thus obtaining a higher sensitivity and a larger dynamic range of the signal. However, this solution is not compatible with plasma chamber conditions so we used the sample current to detect the photoemitted electrons. (2) Their research has predominantly focused on single crystal diamond. However in [36], they observed similar properties between single-crystal and poly-crystalline diamond which suggest the applicability of their analysis to the materials of interest here, i.e. μc-D (poly-crystalline), μc-BDD (poly-crystalline) and PDD (single crystal).

2.4.3. Determining the ionization threshold from measurements of the photocurrent. Fowler fitting [43, 44] is used to determine the ionization threshold from each plot of photocurrent with respect to incident photon energy. The fitting procedure is as detailed in [24]. Briefly, the background current is measured in the absence of incident light at the end of each acquisition. Each curve is shifted such that its background level aligns with that observed in the measurement at room temperature. The background is then removed from the data and the photocurrent is corrected by the spectral response of the optical setup to obtain the photoemission yield P_{Y},

$$P_{\mathrm{Y}} = \frac{I_{\mathrm{ph}}}{F(h\nu)} \tag{1}$$

where I_{Ph} is the photon induced current on the sample and $F(h\nu)$ is the wavelength dependent photon flux of the light incident on the sample.

A Fowler fit is then applied using equation (2). Note that this is an approximation as it is a truncated version of that found in [44]. An example of a Fowler fit is shown in figure 3,

$$P_{\mathrm{Y}} = AT_{\mathrm{s}}^2\left(\frac{\pi^2}{6} + \frac{1}{2}\mu^2 - e^{-\mu}\right) \tag{2}$$

with

$$\mu = \frac{h\nu - \phi}{k_{\mathrm{B}}T_{\mathrm{s}}} \quad , \quad h\nu \geqslant \phi \tag{3}$$

where k_{B} is the Boltzmann constant, T_{s} is the sample temperature, and ϕ is the low ionization threshold. The factor A is made of physical constants and proportionality factors.

Equation (2), using μ to the power 2, keeping A as a constant and ϕ as a fitting parameter is used for the analysis of metals [43]. Due to the varying gradients of photoyield with respect to incident photon energy on our non-metal samples, A has been used as an additional fitting parameter.

The Fowler function is fitted from the lowest photon energy for which the current exceeds the largest noise in the background. A fitting range of 40 nm (corresponding to 20 data

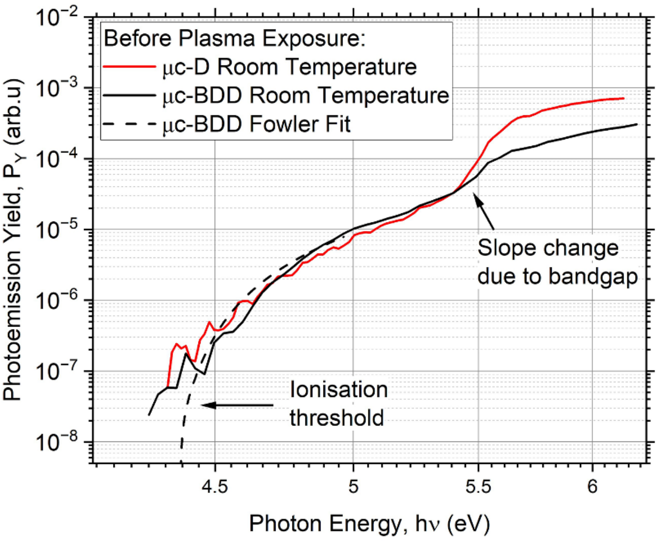

Figure 3. Photoemission yield with respect to incident photon energy before plasma exposure for μc-D and μc-BDD samples at room temperature. The black dotted line represents an example of a Fowler fit to determine the ionization threshold.

points) is used to limit the temperature drop of the sample over the course of the measurement to approximately 20 °C for the highest temperature measurements (600 °C).

Error bars for the ionization threshold ϕ in all cases are calculated as shown in equation (4) to account for the ±5 nm resolution of the monochromator:

$$\Delta\phi = \frac{hc\Delta\lambda}{e\lambda^2} \tag{4}$$

where h is Planck's constant (6.6×10^{-34} Js), c is the speed of light in a vacuum (3×10^8 ms^{-1}), λ is the wavelength of the incident light, and e is the elementary charge (1.6×10^{-19} C).

At 5.5, 4.5, 3.5 and 2.5 eV (225, 276, 354, 496 nm) this represents an energy width of 0.25, 0.16, 0.1 and 0.05 eV, respectively, limiting the threshold determination accuracy on PYS spectra.

2.5. *Experiment protocol for PYS and mass spectrometer*

The measurement procedure was as follows:

- Plasma was ignited in the chamber and left for 30 min to condition the walls (outgas impurities, clean the surface, and adsorb hydrogen) while the sample is left at floating potential ($V_f = 6$ V) such that a steady state plasma is reached and no changes in the plasma-wall interaction take place throughout the measurements. Plasma conditions: inductively coupled plasma using D_2 gas (98% D_2, 2% H_2) at 150 W and 2 Pa with a plasma potential of 7 V.
- The samples were heated to temperature T_s, and pulsed biased at −20 V or −60 V under plasma exposure for 5 min. This is the time after which no change in the work function, and therefore the surface state of the sample, is observed as a result of further ion bombardment from the plasma. It corresponds to a dose of high energy ions (ions accelerated from the plasma potential to the sample biased at −20 V or −60 V during the pulses) of approximately 1.8×10^{19} ions m^{-2} and low energy ions (ions accelerated from the plasma to the sample at ground outside of the pulses) of approximately 8.8×10^{20} ions m^{-2}.
- The small photocurrent could not be measured during the plasma phase due to the high plasma current. The plasma is therefore switched off by stopping the gas supply and setting the RF power to zero.
- The sample bias voltage was removed and the ammeter connected via the switches in figure 1(b). The 7.5 V cone bias was also switched on.
- The heating filament set point, attached to the sample holder to control its temperature to T_s as shown in figure 1(b), was briefly increased so that after switching off the heating, temperature drops were centered around the sample temperature at plasma exposure (e.g. 200 °C would be heated to 205 °C and would drop to 195 °C during acquisition). Approximately 45 s passes between switching the plasma off and starting the measurement of the photocurrent.
- The 35 Hz modulated photocurrent was measured with respect to wavelength of the incident light.

PYS and mass spectrometry measurements were undertaken in an ABBA order as sample temperature was increased, for example, PYS at room temperature, followed by mass spectrometry at room temperature and 200 °C, followed by PYS at 200 °C and 300 °C etc.

As both the plasma and the heating element for the sample are switched off immediately before the measurement of the photocurrent to minimize additional sources of current on the sample, a small temperature drop is incurred during the acquisition. Therefore, a 150 nm wavelength range (in 2 nm steps) close to the threshold in addition to a short, 1 s acquisition time per point is used to minimize sample temperature reduction during the measurement which takes approximately 1 min. This limits the temperature drop to approximately 10 °C at 200 °C and up to 100 °C at 600 °C. PYS acquisitions were not attempted at 700 °C as the temperature drop is too large. These 'short' scans were used to determine the ionization threshold energy. The temperature plotted in figures 9 and 10 refer to the stable sample temperature at which plasma exposure occurred. The limit of detection for determination of the threshold is approximately 80 fA at room temperature and 100 fA at 400 °C.

For the broader wavelength scans displayed in sections 3.1 and 3.2 that are used to determine electronic structure, a 5 nm step size was used to limit the temperature drop during each acquisition. Taking several acquisitions over more narrow wavelength ranges (e.g. 200–300 nm, 300–400 nm and 400–500 nm) and stitching them together produced near identical curves to the single acquisitions taken over the full wavelength range (e.g. 200–500 nm), which suggests that the temperature drop during each full acquisition does not influence the measurements too much.

2.6. Preparation of doped diamond samples

μc-D films were deposited at LSPM laboratory by plasma-assisted chemical vapor deposition (CVD) in a bell jar reactor (PLASSYS BJS 150) operating with a mixture of H_2 and CH_4. The methane concentration was set to 4%. The reactor was operated at 200 mbar pressure, and the injected microwave power was set to 3 kW and the surface temperature was approximately 900 °C. The film was deposited on (100) oriented silicon substrate. The deposited diamond layer had a thickness of 17 μm. After film deposition, the sample was exposed to pure H_2 plasma to ensure hydrogen termination of the sample surface.

μc-BDD samples were purchased from NeoCoat [45]. They were deposited onto silicon substrate using CVD. The μc-BDD layers had a thickness between 2 and 3 μm and a charge carrier density maximum of 2.0×10^{20} cm^{-3}. Both the μc-D and μc-BDD samples have a surface area of 12 × 12 mm^2 and are expected to be hydrogen terminated from the deposition process.

The microcrystalline diamond layers were observed by confocal microscopy. The non-doped diamond layer has a grain size of approximately 10 μm and a roughness at the confocal microscopy scale (100 μm × 100 μm images) of approximately 0.5 μm. The boron-doped diamond layer has a grain size of approximately 0.5 μm and a roughness of approximately 50 nm on the same scale. It should be noted, however, that the grain size in this case is in the lower limit for correct observation by confocal microscopy and that the roughness given is only an estimate, which nevertheless shows a much lower roughness than for the non-doped sample.

A PDD layer was deposited at GEMaC laboratory. GEMaC laboratory has the ability to grow n-type PDD homoepilayers by microwave plasma assisted CVD [46]. The standard process makes use of a metallic reactor for a 3 h period (total gas flow of 1000 sccm, pressure of 50 mbar, growth temperature of 990 °C, gas ratio of 0.05% for $[CH_4]/[H_2]$ and 12% for $[P]/[C]_{gas}$), to grow a conductive PDD layer with a dopant concentration of approximately 2×10^{20} cm^{-3}. Note that while the standard process grows the PDD layer on a polished Sumicrystal type Ib HPHT (111) diamond supplied from Sumitomo (2.0 × 2.0 mm^2, 0.3 mm thick), a larger substrate of type Ib HPHT (111) single crystal diamond substrate purchased from Element 6 (SC Macle Type Ib 4.0 × 4.0 × 3.0 mm, 1.0 mm thick, $<111>$, L2) was used here to allow a larger surface of interaction with the plasma and easier detection of negative-ions. However, the larger substrate presents a larger roughness of approximately 120 nm at an image scale of 10 μm × 10 μm (instead of 1.5 nm on 10 × 10 μm^2 Sumitomo substrates) as measured by atomic force microscopy and without the typical polishing lines on the surface. The phosphorus-doped diamond layer as deposited was not analyzed, but its roughness is probably at least as high as that of the substrate. These differences influenced the growth and led to a single crystal of lower quality than expected. The phosphorus content was analyzed by secondary ion mass spectrometry and was evaluated to be approximately 5×10^{19} cm^{-3} (four times less than expected) within a thickness of approximately 675 nm. The sample has then been chemically de-hydrogenated in order to perform four point-probe measurements. Unfortunately, due to the low dopant concentration, no resistance was measurable (approximately 50 MΩ being the minimum resistance measurable on the set-up).

Finally, let us note that while the plasma-exposed surface area of PDD is smaller than that of μc-BDD and μc-D, modeling has shown that only negative ions coming from an area of approximately 4 mm^2 have the correct angle of incidence to pass through the mass spectrometer and be measured. Therefore the varying surface areas of the samples is not expected to significantly influence the measurements.

3. Results

The results below are split into four sections. First, full wavelength scans (up to a 500 nm range) of PYS are used to determine the electronic structure of the diamond samples before and after plasma exposure in sections 3.1 and 3.2, respectively. Next, the effect of plasma exposure on the low ionization threshold of PDD is characterized in section 3.3. Finally, the simultaneous variation of the low ionization threshold and negative ion production of the diamond samples is shown in section 3.4.

3.1. Electronic structure of diamond before plasma exposure

Figure 3 shows the photoemission yield with respect to incident photon energy for an μc-D and μc-BDD sample before exposure to plasma.

The spectra shown in figure 3 are in close agreement with the ones shown by Takeuchi *et al* [31] with an ionization threshold around 4.4 eV and a change of slope around 5.5 eV. This shows that neither the cleaning and annealing sequence nor the fact that we employ polycrystals instead of single crystals significantly affect the diamond layer properties, and we can use the work of Takeuchi *et al* to help interpret the obtained spectra.

Figure 4 shows the photoexcitation paths on hydrogenated (a) μc-D, (b) μc-BDD, and (c) PDD surfaces [35].

A bandgap of 5.47 eV is present on each of the diamond surfaces shown in figure 4. The dashed lines in figures 4(b) and (c) represent the dopant levels at 0.37 eV above the valence band for μc-BDD, and 0.6 eV below the conduction band for PDD.

In the hypothesis of a positive electron affinity, no electron emission could occur below about 5.47 eV. The appearance of a sub bandgap photoemission in figure 3 is attributed to the NEA of hydrogenated diamond, and a photoemission

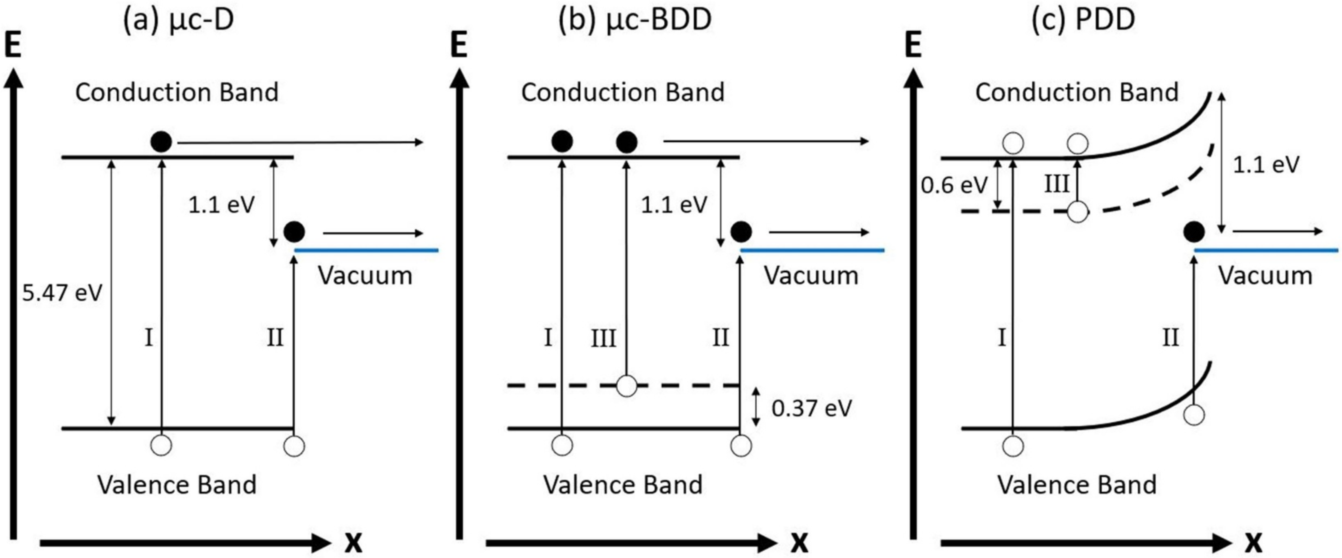

Figure 4. Photoemission mechanisms through electron excitation in the band structures of hydrogenated (a) μc-D, (b) μc-BDD, and (c) PDD. Dashed lines represent the dopant levels. Reprinted from [35], Copyright (2006), with permission from Elsevier.

mechanism in which electrons from the valence band in the immediate proximity of the surface absorb photons and are emitted directly into vacuum, corresponding to mechanism II in figures 4(a) and (b).

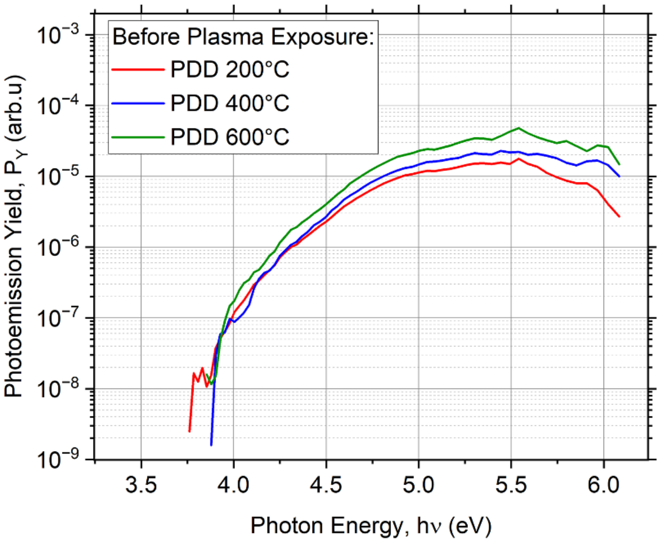

Figure 5. Photoemission yield with respect to incident photon energy before plasma exposure for PDD samples at varying sample temperature. Full spectral range taken in one acquisition at each temperature, corresponding to temperature ranges of approximately 210 °C–190 °C, 420 °C–370 °C and 610 °C–510 °C at 200 °C, 400 °C and 600 °C, respectively.

The electron affinity, which is the energy difference between the vacuum level and the conduction band minimum, can therefore be estimated to be $\chi = -1.1$ eV (ionization threshold minus the bandgap) corresponding to the value obtained by Takeuchi *et al* in [31]. Above the ionization threshold, the signal rises as more and more electrons from the valence band can be emitted into vacuum. As shown in figure 3, for energies larger than 5.4 eV an increase in the photoemission yield is observed, which can be attributed to the creation of excitons by photon absorption in the diamond bulk from the valence band to the conduction band. This occurs over a distance corresponding to the light penetration depth, approximately 10–20 μm [31]. The threshold energy corresponds to the band gap (5.47 eV) minus the exciton ground level binding energy (0.08 eV). The electrons promoted to the conduction band dissipate their energy through inelastic collisions on a sub-picosecond time scale and over approximately 10 nm to end up at the conduction band minimum energy level. The thermalized electrons can then be transported towards the diamond surface with a large escape depth [36], in the range of micrometers (defined by the electron–hole recombination time). For a positive electron affinity material, these electrons would not be emitted into vacuum due to the energy barrier on the surface but for a NEA these 'bulk' electrons can be released to vacuum, shown as mechanism I in figures 4(a) and (b). This mechanism explains the large rise of current at 5.4 eV observed for μc-D and μc-BDD in figure 3. The bandgap is indirect in diamond and the exciton creation occurs through absorption of a photon and phonon emission or absorption. Takeuchi *et al* observed the different thresholds due to phonon absorption or emission [35]. The most intense ones are at 5.26 eV and at 5.54 eV at room temperature. The spectral resolution at 5.5 eV (0.25 eV) might lead to an overlapping of the different thresholds around the bandgap energy leading to the appearance of only one global threshold in the spectra.

Figure 5 shows the photoemission yield with respect to incident photon energy for the non-hydrogenated PDD samples at varying sample temperature before exposure to plasma.

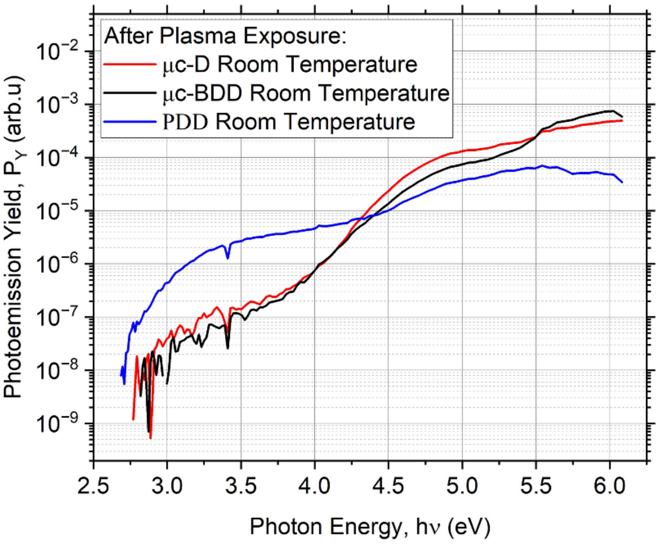

Figure 6. Photoemission yield with respect to incident photon energy after deuterium plasma exposure (2 Pa, 150 W) for μc-D, μc-BDD, and PDD samples pulsed bias at -20 V at room temperature.

Only one ionization threshold of 3.75 eV is detected for all temperatures. An ultraviolet photoelectron spectroscopy measurement was performed at 400 °C to confirm the calibration of the PYS and obtained a threshold of 3.85 eV. The absence of threshold variation with temperature does not suggest there is photoemission from the phosphorous dopant level, which is 0.6 eV below the conduction band minimum and is therefore depleted when the temperature of the sample increases. The PDD sample does not posses NEA before plasma exposure due to the lack of hydrogenation. Therefore, this sub bandgap emission can be attributed to non-diamond phases or to surface defects in the bandgap. Indeed, as it will be shown later on in section 3.2, PDD PYS spectra after plasma exposure, and thus after surface hydrogenation, become very different.

3.2. Electronic structure of diamond after plasma exposure

Figure 6 shows the photoemission yield with respect to photon energy after deuterium plasma exposure at room temperature. A sample bias of -20 V with a pulse length of 20 μs and duty cycle of 2% is used to preserve the surface state, as detailed in section 2.2.

Similar to the situation before plasma exposure, we can observe a signal rise threshold at approximately 5.4–5.5 eV for μc-D and μc-BDD, which is consistent with expectations and corresponds to mechanism I on figures 4(a) and (b). The sub bandgap photoemission shows that diamond layers after deuterium plasma exposure still present NEA at room temperature.

There is another signal rise with a threshold around 3.8 eV. This is a shift of about -0.6 eV compared to the situation before plasma exposure. This could correspond to a decrease of NEA from approximately -1.1 to -1.7 eV.

Finally, there is a new signal contribution with a threshold at around 2.8 eV. This is a rather low signal that could correspond to photoemission from hydrogenated non-diamond phases (sp^2 defects) possibly at grain boundaries. Alternatively, this low threshold could be from surface defect states possibly created by the interaction between the plasma and the surface. These states would be located at 1.5 eV above the valence band maximum if we assume an NEA of -1.1 eV (or 0.9 eV if we have an NEA of -1.7 eV). Takeuchi *et al* observed surface defect states located 1.7 eV above the valence band maximum after partial de-hydrogenation of diamond by thermal annealing [37].

The post plasma spectra of PDD noticeably differs from the pre-exposure spectra. There is a clear rise in signal at 4.4 eV, also observed on μc-D and μc-BDD prior to plasma exposure and which has been attributed by Takeuchi *et al* to the mechanism II of photoemission in figure 4(c) [31]. This shows that the deuterated PDD sample is now presenting NEA of -1.1 eV, as expected from hydrogenated diamond [31].

The absence of signal threshold around 5.5 eV was also noticed by Takeuchi *et al* and explained by a positive band bending on the surface preventing electrons in the conduction band from escaping into vacuum and thus canceling the possibility of photoemission through mechanism I in figure 4(c). The origin of the positive band bending was not elucidated but it was suggested that it could be due to a space charge generated by a layer of ionized phosphorous donors in the vicinity of the surface due to electron emission in vacuum [31]. Finally, a clear signal contribution is observed below 4.4 eV with a threshold at 2.6 eV. We suggest that this is from the phosphorous donors in the vicinity of the surface.

Figure 7 shows the photoemission yield with respect to photon energy after deuterium plasma exposure at 400 °C.

Only two signal thresholds are observed in the PYS spectra of μc-BDD after plasma exposure at 400 °C, shown in figure 7, one corresponding to the interband mechanism of emission at about 5.2 eV and one corresponding to direct emission of electrons in the vicinity of the surface towards vacuum with a threshold at 3.8 eV. It is known that sp^2 phases are preferentially etched compared to sp^3 phases when increasing the temperature above room temperature [47]. At 400 °C, the absence of a signal contribution with a threshold at 2.9 eV (observed after exposure at room temperature) suggests that this threshold at low energy is due to hydrogenated sp^2 defects created by ion bombardment. We have also observed that at 600 °C the threshold reaches approximately 4.2 eV with a similar curve shape to the before plasma exposure acquisition, showing that as we anneal at higher temperatures, the sample surface returns closer to its pre-exposed state (4.4 eV threshold). The same holds true for μc-D but there is still a small contribution at lower energy (threshold at around 3.3 eV at 400 °C). This may suggest that some defects that contributed to the 2.9 eV threshold at room temperature may remain in the μc-D sample even after annealing at 400 °C.

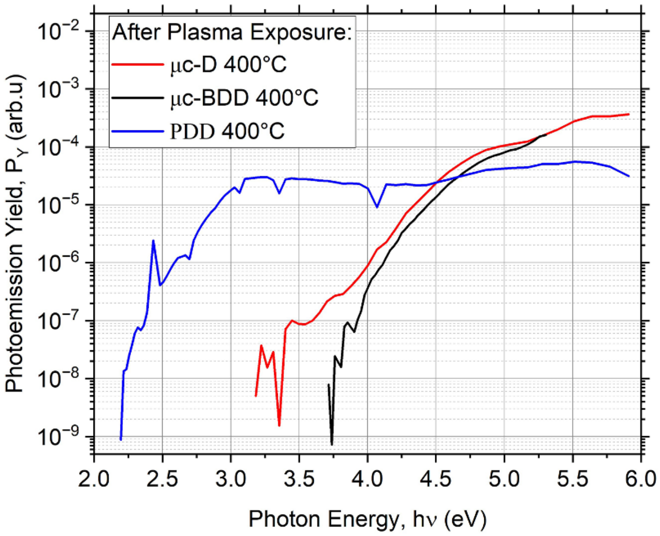

Figure 7. Photoemission yield with respect to incident photon energy after deuterium plasma exposure (2 Pa, 150 W) for μc-D, μc-BDD, and PDD samples pulsed bias at -20 V at 400 °C.

For PDD at 400 °C, figure 7, the low energy threshold is shifted to 2.2 eV. The shift to lower energies, unlike μc-D and μc-BDD, even with the additional annealing present at 400 °C supports the hypothesis that this extremely low energy threshold is driven by the phosphorus as opposed to defects. We suggest that this shift is due to the increase in ionization of the phosphorus donors at 400 °C, leading to electron emission from the conduction band minimum. It is interesting to note that the signal threshold at 4.4 eV is still observed at 400 °C, demonstrating that the NEA has not changed ($\chi = -1.1$ eV).

3.3. Determining the low ionization threshold of plasma-exposed phosphorous doped diamond

Figure 8 shows changes in the low ionization threshold of PDD with respect to sample temperature.

Figure 8(a) shows that at approximately 70 °C the ionization threshold is 2.4 eV, this falls to around 2.1 eV at 400 °C before rising again to 2.4 eV at 600 °C. As the minimum ionization threshold was observed at 400 °C, the negative ion yield is expected to be optimized around this temperature. This value of 2.1 eV is of particular significance as it matches that of bulk cesium [41, 48], even if caesiated materials of optimal deposition thickness can achieve much lower ionization thresholds [49, 50].

The ionization thresholds in figure 8(b) are determined from the PDD sample as it cools and is reheated without further exposure after an initial exposure to plasma at a sample temperature of 400 °C. Data point 1 shows the optimal ionization threshold of 2.1 eV straight after plasma exposure at 400 °C. Without further plasma exposure, the threshold is seen to continuously increase up to 2.5 eV for data points 2–7 as the sample cools to around 120 °C. These points are taken at arbitrary intervals as it cools and point 7 is conducted around 25 min after point 1. For data point 8 it is subsequently reheated to 400 °C without further plasma exposure and returns to 2.1 eV. After allowing the sample to return to room temperature and rest for approximately 18 h, the ionization energy increases to 2.8 eV at data point 9 and then returns to 2.1 eV at data point 10 after reheating to 400 °C. This shows both the repeatability of the measurements, and that the surface state of the material created by exposure to a 400 °C deuterium plasma remains stable for at least 18 h when held at a vacuum of approximately 2×10^{-8} mbar.

The observed variation in the ionization threshold as the temperature of the sample changes, figure 8(b), may be due to the variation of the fraction of ionized phosphorous donors and to the limit of detection of the photoemission diagnostic. First, we assume that 2.7 eV is the threshold for photoemission from the P donors in the vicinity of the surface directly to vacuum, i.e. there is a 2.7 eV gap between the phosphorus dopant level and the vacuum level due to band bending. Then, 2.1 eV would be the threshold for photoemission from the conduction band minimum to vacuum since the P donor energy level is 0.6 eV below the conduction band minimum [29]. Between 2.1 and 2.7 eV the photoemission signal can only come from electrons emitted from the conduction band minimum. The number of electrons at the conduction band minimum is set by the number of ionized P donors which itself is depending exponentially on the temperature. When the number of electrons at the conduction band minimum is too low (at low sample temperature), the photoemission signal at 2.1 eV is below the detection limit giving an apparent signal threshold at higher energy. This explains the shift in the signal threshold with temperature.

In figure 8(a) we can see that after plasma exposure at room temperature the ionization energy is 2.4 eV. In contrast, in figure 8(b) the ionization energy of the PDD sample at room temperature after exposure to plasma at 400 °C is 2.7 eV. This suggests that the final surface state, and hence the ionization threshold, is determined by a coupling of plasma exposure and sample temperature during exposure.

3.4. Ionization threshold and negative ion variation with temperature

Figure 9 shows the negative ion counts and ionization threshold variation of μc-D, μc-BDD, and PDD with respect to sample temperature for -20 V pulsed bias samples.

The negative ion counts as measured using a mass spectrometer for each material in figure 9(a) show different variations with sample temperature but all converge towards approximately 2×10^5 counts from around 400 °C and above. μc-D is seen to decrease with temperature, starting at around 3.8×10^5 counts at room temperature and finishing with 1.9×10^5 counts at 700 °C. μc-BDD takes the form of a relatively flat peak structure with 1.6×10^5 counts at room temperature, increasing to a peak of 2.3×10^5 at 400 °C and subsequently reducing to

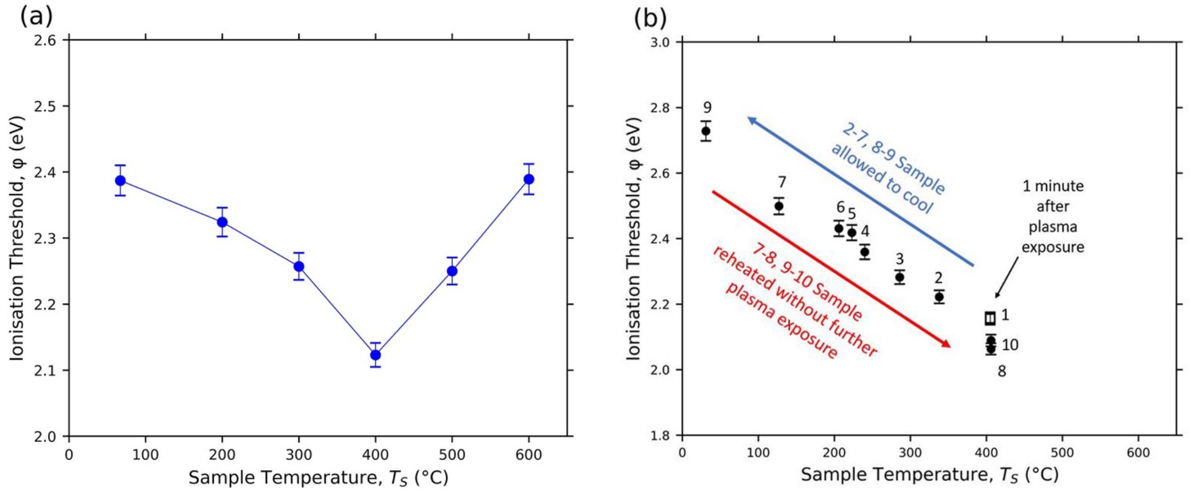

Figure 8. (a) Ionization threshold of PDD when exposed to plasma at varying sample temperature. (b) Ionization threshold variation of PDD when exposed to plasma at 400 °C followed by cooling and reheating of sample without further plasma exposure. Numbers 1–10 represent the chronological order of the measurements with point 1 starting approximately one minute after plasma exposure. D_2 plasma at 150 W and 2 Pa with a −20 V pulsed sample bias.

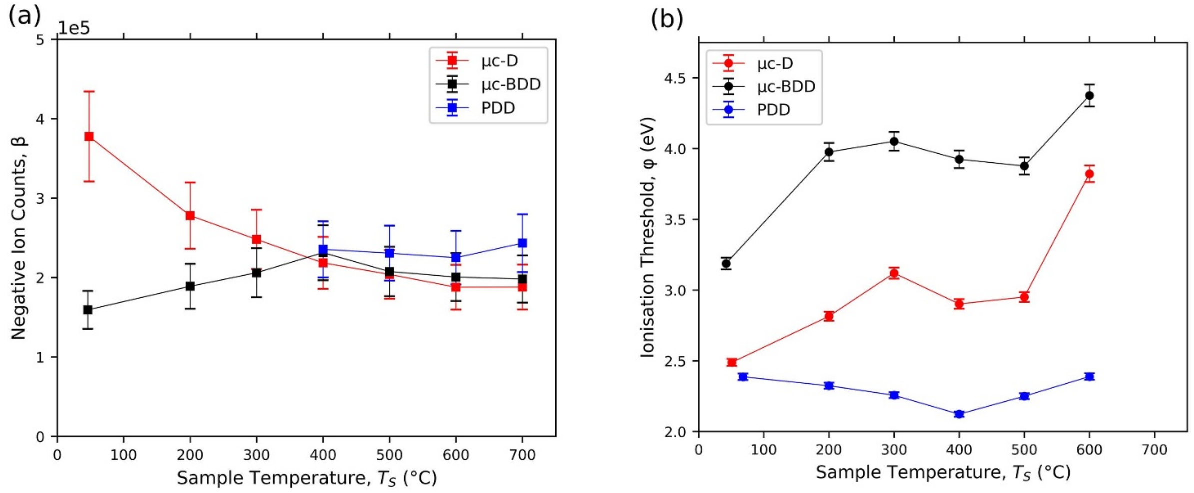

Figure 9. μc-D, μc-BDD, and PDD (a) negative ion counts and (b) ionization threshold with respect to sample temperature at −20 V pulsed sample bias, showing the case with negligible sputtering yield. D_2 plasma at 150 W and 2 Pa. Solid lines have been added as a visual guide.

2.0×10^5 counts at 700 °C. PDD remains approximately constant between 2.2×10^5 and 2.4×10^5 counts over the range of 400 °C–700 °C.

It is important to note that negative ion measurements of PDD at sample temperatures of 300 °C and below are not included in either the −20 V or −60 V case. This is because there are an insufficient number of electrons in the conduction band to ensure conductivity high enough to enable biasing of the sample. The capacitance between the sample and the sample holder is too high to allow biasing of the non-conductive PDD sample as explained in [21]. At around 400 °C and above, a sufficient number of electrons from the phosphorus dopant level (0.6 eV below the conduction band) begin to populate the conduction band, allowing for sample biasing. The μc-D and μc-BDD samples can be bias at all temperatures.

The ionization threshold for each material in figure 9(b) also shows distinct variations with temperature. μc-D has a ionization threshold of 2.5 eV at room temperature, this increases to 3.1 eV at 300 °C before a slight decrease to 2.9 eV at 400 °C–500 °C and large increase to 3.8 eV at 600 °C. μc-BDD shows a very similar trend only shifted higher by approximately 0.7 eV at all temperatures. In contrast, PDD starts at 2.4 eV at room temperature and gradually falls to 2.1 eV (equivalent to that of cesium) at 400 °C before increasing back to 2.4 eV at 600 °C.

Figure 10 shows the negative ion counts and ionization threshold variation of μc-D, μc-BDD, and PDD with respect to sample temperature when biased at −60 V.

The negative ion counts for μc-D and μc-BDD in 10(a) both appear to have a broad peak with respect to sample temperature. μc-D has 1.1×10^6 counts at room temperature

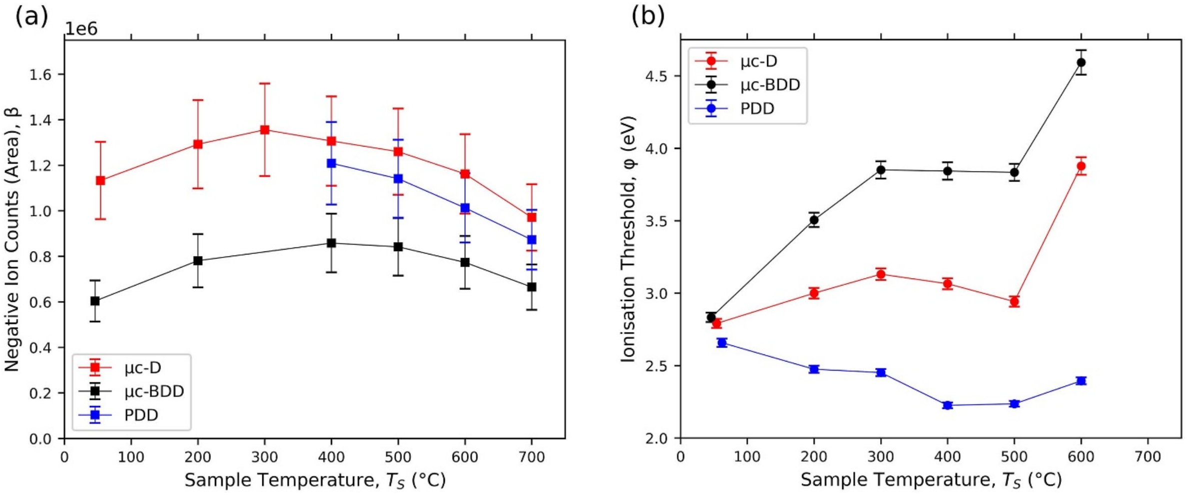

Figure 10. μc-D, μc-BDD, and PDD (a) negative ion counts and (b) ionization threshold with respect to sample temperature at −60 V pulsed sample bias, showing the case with sputtering contribution. D_2 plasma at 150 W and 2 Pa. Solid lines have been added as a visual guide.

before peaking at 1.4×10^6 counts at 300 °C and decreasing to 1.0×10^6 counts at 700 °C. μc-BDD displays a similar trend, increasing from 6.0×10^5 counts up to 9.0×10^5 counts at 400 °C and back to 7.0×10^5 counts at 700 °C. PDD has an maximum value of 1.2×10^6 counts at 400 °C and subsequently decreases to 9.0×10^5 counts at 700 °C.

As in the −20 V case, the ionization threshold variation with sample temperature of μc-D and μc-BDD in figure 10(b) are similar. μc-D increases from 2.8 eV at 61 °C to 3.1 eV at 300 °C, back down to 2.9 eV at 500 °C and then a significant increase up to 3.9 eV at 600 °C. μc-BDD also starts at 2.8 eV but increases to a much higher value of 3.8 eV at 300 °C–500 °C before increasing to 4.6 eV at 600 °C. Also following a similar trend to the −20 V case, PDD starts at 2.7 eV at room temperature, decreases down to 2.2 eV at 400 °C and 500 °C and then re-increases to 2.4 eV at 600 °C.

Figures 9(b) and 10(b) show that the doping of μc-D has a clear and significant effect on the ionization threshold of the plasma exposed layers. The p-type doping with boron increases the ionization threshold while the n-type doping with phosphorus decreases the ionization threshold. In the most extreme cases presented, this can vary the ionization threshold between 2.1 eV and 4.6 eV. It is also clear when compared to the negative ion counts that this variation is not the primary factor in negative ion production. For example, at 500 °C in the −20 V case, ionization thresholds of 3.0 eV, 3.9 eV, and 2.3 eV for μc-D, μc-BDD, and PDD, respectively all result in a similar number of negative ion counts. The ionization threshold of each material is seen to be similar in the −20 V and −60 V cases. This could either be because ion bombardment energy has little effect on the surface state, or the 2% duty cycle allows insufficient bombardment time for this to take effect.

The broad peaks for μc-D and μc-BDD in figure 10(a) are in agreement with the trends seen in previous work [19, 24]. In [24], the varying ionization threshold with temperature of μc-BDD was not seen to have any clear effect on the negative ion yield, the same is observed in figures 9 and 10. Previous modeling has shown that the sub-surface hydrogen content in diamond increases between room temperature and 400 °C, and then decreases at higher temperatures [19, 25]. Therefore, the initial increase in negative ion yield up to approximately 400 °C can be attributed to an increase in sub-surface hydrogen content, increasing the production of negative ions through sputtering. Similarly, the subsequent decrease is thought to be either the increasing ionization threshold or outgassing of adsorbed hydrogen, leading to a reduction in negative ion production from sputtering. The plateauing negative ion counts at −20 V, where the ion bombardment energy is too low to induce significant sputtering, compared to a continuous decrease above approximately 400 °C for all three materials at −60 V suggests it is the outgassing of adsorbed hydrogen causing the decrease of negative ion counts at higher temperatures. Note that this outgassing refers to the removal of excess hydrogen, and does not necessarily imply that the top surface is no longer hydrogen terminated. The cause for the larger negative ion counts from μc-D relative to μc-BDD below 400 °C in figure 9 and at all temperatures in figure 10(a) is unknown.

The lack of influence of the low ionization threshold on negative ion production may be due to the low density of states in dopant, defect and conduction band states, although the effect of the density of states on negative ion production is yet to be fully investigated. This implies that the majority of electron capture for negative ion production comes from the valence band, which means that very little difference is seen between the μc-D, μc-BDD, and PDD samples. This suggests that for negative ion production from dielectrics, the ideal material would have as large an NEA as possible (i.e. the vacuum level is as close to the valence band as possible) and a wide band gap to suppress electron loss back to the surface.

4. Conclusion

We have investigated the effect of low pressure deuterium plasma exposure (150 W, 2 Pa) on the electronic structure and ionization threshold of doped diamond at varying sample temperatures (30 °C–700 °C) and the effect this has on negative ion production. PYS and mass spectrometry were used, respectively, to determine the ionization threshold and measure the production of negative ions. All of the hydrogenated diamond samples (μc-D, μc-BDD and PDD) display NEA. Plasma exposure is seen to significantly reduce the ionization threshold in all cases, likely through ion impact induced defect states created in the band gap and possibly a shift of NEA in μc-D and μc-BDD, and through electrons emitted from phosphorus donors in the vicinity of the surface for PDD. Large variations in the low ionization threshold with sample temperature and between the doped diamond samples (approximately 2 eV shift between BDD and PDD) are observed to have negligible effect on negative ion production, suggesting other parameters such as adsorbed hydrogen, defect production, and the density of states at each threshold energy may be more important.

Data availability statement

The data that support the findings of this study are openly available at the following URL/DOI: https://doi.org/10.15124/19b0662e-0c26-422b-bf96-ec43431b8fab.

Acknowledgments

This work has been carried out within the framework of the French Federation for Magnetic Fusion Studies (FR-FCM). The project that gave rise to this publication received funding from the Initiative of Excellence of Aix-Marseille University—A*Midex, Investissements d'Avenir program AMX-19-IET-013. This project has also been supported by the Région Sud PACA through the Appel à projets recherche 2021 - Volet exploratoire—project SARDINE. This research was funded by the Agence Nationale de la Recherche (ANR) under project 'ANR-23-CE30-0025-01'. The financial support of the EPSRC Centre for Doctoral Training in fusion energy is gratefully acknowledged under financial code EP/S022430/1.

ORCID iDs

Ryan Magee https://orcid.org/0000-0003-4153-5346
Marie-Amandine Pinault-Thaury https://orcid.org/0000-0001-7843-9935
Jocelyn Achard https://orcid.org/0000-0001-7000-7230
Marco Minissale https://orcid.org/0000-0001-6331-1402
Timo Gans https://orcid.org/0000-0003-1362-8000
James P Dedrick https://orcid.org/0000-0003-4353-104X
Gilles Cartry https://orcid.org/0000-0002-6081-0350

References

[1] Vozniy O V and Yeom G Y 2009 High-energy negative ion beam obtained from pulsed inductively coupled plasma for charge-free etching process *Appl. Phys. Lett.* **94** 1–4
[2] Donnelly V M and Kornblit A 2013 Plasma etching: yesterday, today and tomorrow *J. Vac. Sci. Technol.* A **31** 050825
[3] Ueno A, Oguri H, Ikegami K, Namekawa Y and Ohkoshi K 2010 Interesting experimental results in Japan proton accelerator research complex H^- ion-source development (invited) *Rev. Sci. Instrum.* **81** 1–7
[4] Peters J 2000 Negative ion sources for high energy accelerators (invited) *Rev. Sci. Instrum.* **71** 1069–74
[5] Moehs D P, Peters J and Sherman J 2005 Negative hydrogen ion sources for accelerators *IEEE Trans. Plasma Sci.* **33** 1786–98
[6] Faircloth D and Lawrie S 2018 An overview of negative hydrogen ion sources for accelerators *New J. Phys.* **20** 025007
[7] Rafalskyi D and Aanesland A 2016 Brief review on plasma propulsion with neutralizer-free systems *Plasma Sources Sci. Technol.* **25** 043001
[8] Lafleur T, Rafalskyi D and Aanesland A 2015 Alternate extraction and acceleration of positive and negative ions from a gridded plasma source *Plasma Sources Sci. Technol.* **24** 015005
[9] Aanesland A, Rafalskyi D, Bredin J, Grondein P, Oudini N, Chabert P, Levko D, Garrigues L and Hagelaar G 2015 The PEGASES gridded ion-ion thruster performance and predictions *IEEE Trans. Plasma Sci.* **43** 321–6
[10] Fantz U, Wünderlich D, Riedl R, Heinemann B and Bonomo F 2020 Achievement of the ITER NBI ion source parameters for hydrogen at the test facility ELISE and present Status for deuterium *Fusion Eng. Des.* **156** 111609
[11] Hemsworth R S *et al* 2017 Overview of the design of the ITER heating neutral beam injectors *New J. Phys.* **19** 025005
[12] Bacal M and Wada M 2015 Negative hydrogen ion production mechanisms *Appl. Phys. Rev.* **2** 021305
[13] Santoso J, Manoharan R, O'Byrne S and Corr C S 2015 Negative hydrogen ion production in a helicon plasma source *Phys. Plasmas* **22** 093513
[14] Hemsworth R *et al* 2009 Status of the ITER heating neutral beam system *Nucl. Fusion* **49** 045006
[15] Fantz U, Franzen P and Wünderlich D 2012 Development of negative hydrogen ion sources for fusion: Experiments and modelling *Chem. Phys.* **398** 7–16
[16] Bacal M, McAdams R and Surrey E 2014 Extracted H^- ion current enhancement due to caesium seeding at different plasma grid bias *Rev. Sci. Instrum.* **85** 02B103
[17] Hemsworth R S and Boilson D 2019 Research, design and development needed to realise a neautral beam injection system for a fusion reactor *Fusion Energy* (intechopen)
[18] Sasao M, Moussaoui R, Kogut D, Ellis J, Cartry G, Wada M, Tsumori K and Hosono H 2018 Negative-hydrogen-ion production from a nanoporous $12CaO.7Al_2O_3$ electride surface *Appl. Phys. Express* **11** 066201
[19] Cartry G *et al* 2017 Alternative solutions to caesium in negative-ion sources: a study of negative-ion surface production on diamond in H2/D2 plasmas *New J. Phys.* **19** 025010
[20] Smith G J, Ellis J, Moussaoui R, Pardanaud C, Martin C, Achard J, Issaoui R, Gans T, Dedrick J P and Cartry G 2020

Enhancing surface production of negative ions using nitrogen doped diamond in a deuterium plasma *J. Phys. D: Appl. Phys.* **53** 465204

[21] Smith G J, Tahri L, Achard J, Issaoui R, Gans T, Dedrick J P and Cartry G 2021 Surface production of negative ions from pulse-biased nitrogen doped diamond within a low-pressure deuterium plasma *J. Phys. D: Appl. Phys.* **54** 435201

[22] Kogut D *et al* 2018 Single-crystal and polycrystalline diamond erosion studies in Pilot-PSI *J. Nucl. Mater.* **500** 110–8

[23] Taccogna F *et al* 2021 Latest experimental and theoretical advances in the production of negative ions in caesium-free plasmas *Eur. Phys. J. D* **75** 227

[24] Magee R, Maurice B, Demiane J, Layet J M, Gans T, Dedrick J P and Cartry G 2023 Surface production of negative deuterium ions from plasma-exposed boron doped diamond and graphite: work function measurements using photoemission yield spectroscopy *Plasma Sources Sci. Technol.* **32** 75021

[25] Ahmad A, Pardanaud C, Carrère M, Layet J M, Gicquel A, Kumar P, Eon D, Jaoul C, Engeln R and Cartry G 2014 Negative-ion production on carbon materials in hydrogen plasma: influence of the carbon hybridization state and the hydrogen content on H^- yield *J. Phys. D: Appl. Phys.* **47** 085201

[26] Kumar P, Ahmad A, Pardanaud C, Carrère M, Layet J M, Cartry G, Silva F, Gicquel A and Engeln R 2011 Enhanced negative ion yields on diamond surfaces at elevated temperatures *J. Phys. D: Appl. Phys.* **44** 372002

[27] Koeck F A M, Nemanich R J, Lazea A and Haenen K 2009 Thermionic electron emission from low work-function phosphorus doped diamond films *Diam. Relat. Mater.* **18** 789–91

[28] Kato H, Takeuchi D, Ogura M, Yamada T, Kataoka M, Kimura Y, Sobue S, Nebel C E and Yamasaki S 2016 Heavily phosphorus-doped nano-crystalline diamond electrode for thermionic emission application *Diam. Relat. Mater.* **63** 165–8

[29] Gheeraert E, Koizumi S, Teraji T and Kanda H 2000 Electronic transitions of electrons bound to phosphorus donors in diamond *Solid State Commun.* **113** 577–80

[30] Takeuchi D, Riedel M, Ristein J and Ley L 2003 Surface band bending and surface conductivity of hydrogenated diamond *Phys. Rev.* B **68** 1–4

[31] Takeuchi D, Kato H, Ri G S, Yamada T, Vinod P R, Hwang D, Nebel C E, Okushi H and Yamasaki S 2005 Direct observation of negative electron affinity in hydrogen-terminated diamond surfaces *Appl. Phys. Lett.* **86** 1–3

[32] Takeuchi D, Ri S G, Kato H, Nebel C E and Yamasaki S 2005 Negative electron affinity on hydrogen terminated diamond *Physica Status Solidi* a **202** 2098–103

[33] Takeuchi D, Ri S G, Kato H, Nebel C E and Yamasaki S 2005 Total photoyield experiments on hydrogen terminated n-type diamond *Diam. Relat. Mater.* **14** 2019–22

[34] Takeuchi D, Nebel C E and Yamasaki S 2006 Photoelectron emission from diamond *Physica Status Solidi* a **203** 3100–6

[35] Takeuchi D, Ri S G, Kato H, Nebel C E and Yamasaki S 2006 Secondary photoelectron emission experiments on p-, intrinsic and n-type diamond *Diam. Relat. Mater.* **15** 698–702

[36] Takeuchi D, Saeki K, Christoph E N, Yamasaki S and Oliver A W 2006 Photoelectron emission mechanism from hydrogen terminated nano-crystalline diamond *MRS Online Proc. Libr.* **956** 1–6

[37] Takeuchi D, Nebel C E and Yamasaki S 2007 Surface defect states analysis on diamond by photoelectron emission yield experiments *Diam. Relat. Mater.* **16** 823–5

[38] Takeuchi D, Ogura M, Ri S G, Kato H, Okushi H and Yamasaki S 2008 Electron emission suppression from hydrogen-terminated n-type diamond *Diam. Relat. Mater.* **17** 986–8

[39] Kogut D, Moussaoui R, Ning N, Faure J B, Layet J M, Farley T, Achard J, Gicquel A and Cartry G 2019 Impact of positive ion energy on carbon-surface production of negative ions in deuterium plasmas *J. Phys. D: Appl. Phys.* **52** 1–26

[40] Dudnikov V 2012 Forty years of surface plasma source development *Rev. Sci. Instrum.* **83** 02A708

[41] Cristofaro S, Friedl R and Fantz U 2020 Correlation of Cs flux and work function of a converter surface during long plasma exposure for negative ion sources in view of ITER *Plasma Res. Express* **2** 035009

[42] Achkasov K, Moussaoui R, Kogut D, Garabedian E, Layet J M, Simonin A, Gicquel A, Achard J, Boussadi A and Cartry G 2019 Pulsed DC bias for the study of negative-ion production on surfaces of insulating materials in low pressure hydrogen plasmas *J. Appl. Phys.* **125** 033303

[43] Fowler R 1931 The analysis of photoelectric sensitivity curves for clean metals at various temperatures *Encyclopedia of Neuroscience* vol 107 (https://doi.org/10.1007/978-3-540-29678-2_2920)

[44] Friedl R 2016 Enhancing the accuracy of the Fowler method for monitoring non-constant work functions *Rev. Sci. Instrum.* **87** 043901

[45] NeoCoat we grow diamond (available at: www.neocoat.ch/en)

[46] Pinault-Thaury M A, Tillocher T, Habka N, Kobor D, Jomard F, Chevallier J and Barjon J 2011 N-Type CVD diamond: epitaxy and doping *Mater. Sci. Eng.* B **176** 1401–8

[47] Yamazaki Y, Ishikawa K, Mizuochi N and Yamasaki S 2006 Structure of diamond surface defective layer damaged by hydrogen ion beam exposure *Diam. Relat. Mater.* **15** 703–6

[48] Michaelson H B 1977 The work function of the elements and its periodicity *J. Appl. Phys.* **48** 4729–33

[49] Swanson L W and Sirayer R W 1968 Field-electron-microscopy studies of cesium layers on various refractory metals: work function change *J. Chem. Phys.* **48** 2421–42

[50] Wilson R G 1966 Electron and ion emission from polycrystalline surfaces of Be, Ti, Cr, Ni, Cu, Pt and type-304 stainless steel in cesium vapor *J. Appl. Phys.* **37** 3161–9